

# Nonlinear Distortion Radiated from Large Arrays and Active Reconfigurable Intelligent Surfaces

Nikolaos Kolomvakis, Alva Kosasih and Emil Björnson, *Fellow, IEEE*

**Abstract**—Extremely large aperture arrays (ELAAs) and reconfigurable intelligent surfaces (RISs) are candidate enablers to realize connectivity goals for the sixth-generation (6G) wireless networks. For instance, ELAAs can provide orders-of-magnitude higher area throughput compared to what massive multiple-input multiple-output (MIMO) can deliver through spatial multiplexing, while RISs can improve the propagation conditions over wireless channels but a passively reflecting RIS must be large to be effective. Active RIS with amplifiers can deal with this issue. In this paper, we study the distortion created by nonlinear amplifiers in both ELAAs and active RIS. We analytically obtain the angular directions and depth of the nonlinear distortion in both near- and far-field channels. The results are demonstrated numerically and we conclude that non-linearities can both create in-band and out-of-band distortion that is beamformed in entirely new directions and distances from the transmitter.

**Index Terms**—Extremely large aperture array, reconfigurable intelligent surface, large intelligent surface, uniform planar array, near-field, far-field, nonlinear distortion.

## I. INTRODUCTION

EXTREMELY large aperture arrays (ELAAs) and reconfigurable intelligent surfaces (RISs) are promising technologies for the next generation of wireless systems. These are electrically large arrays respectively used for transmission/reception and reflection. The aim of deploying ELAAs is to provide orders-of-magnitude higher area throughput in wireless networks compared to what massive multiple-input multiple-output (MIMO) can practically deliver. The keys to reaching this goal are the even larger number of antennas and huge apertures that place the users in the radiative near-field, which reduces the average propagation loss and increases the spatial resolution by controlling beams in the depth domain [2].

On the other hand, RISs can turn wireless propagation channels into programmable smart environments by software-controlled reflection of impinging signals [3], [4]. The aim can be to boost the received signal power at the receiver and improve other desired channel properties such as the MIMO channel rank. The basic idea is to densify the next generation of wireless networks with RISs instead of base stations (BSs) to create a low-cost, low-power, and high-throughput communication infrastructure. This new architecture

is characterized by being programmable and reconfigurable, not only at the infrastructure nodes and user devices, but also in the surrounding wireless environment, properly shaped by programmable RISs. Each RIS acts as an advanced kind of transparent full-duplex relay/repeater [5]. Each antenna element of a RIS can be made of metamaterial, acts as an isotropic scatterer when it is sub-wavelength-sized, and the impedance can be tuned by diodes to create an inhomogeneous phase-shift pattern over the surface that reflects an incident wave as a beam in a desirable direction [6].

A conventional *passive RIS* reflects signals without amplification. This has the benefit of low power consumption but requires a large aperture size since the pathloss is the product of the pathlosses to and from the array, while the array gain grows quadratically with the aperture area [6]. Nevertheless, in practice, the capacity gains are typically only substantial in setups where the direct link between transmitter and receiver is completely blocked or very weak [7]. To expand the usefulness of the RIS technology to scenarios where the direct link is not weak, in [8], a new RIS architecture called *active RISs* was proposed to overcome the large path loss of reflected links. The key feature of active RISs is their ability to actively reflect signals with amplification. This can be realized by integrating a reflection-type amplifier into each reflecting element. Different from conventional relays, an active RIS remains to be transparent and full duplex.

The use of low-cost, small-size, and power-efficient hardware is desirable to make ELAA and active RISs sustainable technological shifts, otherwise the cost will increase with the number of antennas. However, decreasing the hardware cost and size as well as increasing its power efficiency typically implies various radio-frequency (RF) imperfections. This issue has been raising increasing interest in the last decade with the advent of massive MIMO systems [9]–[12], including, e.g., the impacts of quantization noise in converters, oscillator phase noise, transceiver I/Q imbalances, and amplifier nonlinearities. For example, practical power amplifiers (PAs) introduce both in-band and out-of-band distortion due to their nonlinear transfer function. This is an undesired feature that is particularly present in low-cost and high-efficiency components [13]. When the input signal to the amplifier exhibits large amplitude variations, the non-linearities in the PAs may create severe spatial distortions.

### A. Relevant Prior Art

The most relevant multi-antenna works are [12], [14], [15]. When it comes to MIMO arrays, only uniform linear arrays

N. Kolomvakis, A. Kosasih and E. Björnson are with the Division of Communication Systems, KTH Royal Institute of Technology, 164 40 Stockholm, Sweden (e-mail: {nikkol, kosasih, emilbj}@kth.se).

This work was supported by the Swedish Governmental Agency for Innovation Systems (VINNOVA).

Parts of this paper have been submitted for potential publication at the European Conference on Antennas and Propagation (EuCAP), Glasgow, Scotland, 2024 [1].

(ULAs) have been analyzed operating in the far-field region. Specifically, [14] showed that in single-user beamforming, nonlinear distortion is beamformed into the same direction as the desired signal, while in multi-user beamforming, the distortion is beamformed into many distinct directions different from those of the desired signals. Moreover, [12] showed that, if the input signal to the amplifiers has a dominant beam, the distortion is beamformed in the same way as that beam. When a superposition of multiple beams is transmitted without anyone being dominant, the distortion is practically isotropic. The transmission over frequency-selective channels gives rise to similar phenomena [15].

### B. Contributions

Although the behavioral modeling of distortion has been studied in the multi-antenna literature, to the best of our knowledge, its effects on ELAAs and active RISs operating in the near-field region have not been addressed before, except in the preliminary version [1] of this manuscript, which studied only active RISs but operating in the far-field region. In this paper, we analyze the distortion either transmitted by an ELAA or created by an active RIS that reflects multiple signals. In both cases, the arrays are configured as uniform planar arrays (UPAs) and we consider operation in both the radiative near-field and far-field regions. Our main contributions can be summarized as follows:

- We analyze the nonlinear distortion radiated from a transmitter (i.e., either ELAA or active RIS) equipped with a UPA. This setup enables us to analyze the distortion in both the azimuth and elevation domains.
- We consider near-field compliant channel models that enable us to analyze the nonlinear distortion in the radiative near-field, where the depth domain can be controlled. In combination with the assumption of a transmitter equipped with a UPA, it provides us with the 3D behavioral analysis of distortion in the entire space of the channel, that is, in the azimuth, elevation and depth domains.
- We derive a theorem that analytically characterizes the angular directions as well as the depth of nonlinear distortion in the near-field region. The theory can be used in system design to predict the effects of the nonlinear distortion and to take distortion effects into account when scheduling users in space and frequency.
- We refine the number of nonlinear distortion directions that were derived in [12] for the far-field. Specifically, it was stated in [12, Th. 2] that third-degree non-linear distortion is beamformed in  $(K^3 - K^2 + 2K)/2$  directions. However, we show that this number is an upper bound and the exact number of directions can be substantially lower than that. Our results hold for both the near-field and far-field regions.

Our analytical and numerical results reveal that when an ELAA (active RIS) transmits (receives) data signals to (from) multiple users, the transmitted (reflected) signal can be distorted by its PAs and its spatial characteristics depend on the position of the users. As an example, the azimuth position of the users

does not affect the beamforming directions of distortion on the elevation domain. However, the position of users in the elevation domain can affect the directions of distortion in the azimuth domain. Finally, when the users are located at different near-field distances from the ELAA or RIS, then the distortion is focused at distinct distances which are different from those of the position of the users.

### C. Notation

Lowercase and uppercase boldface letters denote column vectors and matrices, respectively. For a matrix  $\mathbf{A}$ , we denote its complex conjugate and transpose by  $\mathbf{A}^*$  and  $\mathbf{A}^T$ , respectively. The cardinality of a set  $\mathcal{S}$ , it is denoted as  $|\mathcal{S}|$  which is the number of members of  $\mathcal{S}$ . For a vector  $\mathbf{v} \in \mathbb{C}^N$ , we use  $\text{diag}(\mathbf{v})$  to denote an  $N \times N$  diagonal matrix with the elements of vector  $\mathbf{v}$  being its main diagonal. Finally, we use  $\|\cdot\|$  to denote the  $l_2$ -norm of a vector.

### D. Paper Outline

The rest of the paper is organized as follows. In Section II, we introduce the system model of ELAAs as well as the propagation model for the radiative near-field channel. In Section III, we provide the analytical approximations of distortion's angular directions and depth in Fresnel region as well as analyze the distortion's behaviour in ELAA systems. In Section IV, we revise the nonlinear distortion's analysis assuming an active RIS. In Section V, we provide numerical results and validate the accuracy of our approximations for different scenarios. The paper is concluded in Section VI.

## II. SYSTEM MODEL

We consider a single-cell MIMO-Orthogonal Frequency Division Multiplexing (OFDM) system where an ELAA serves  $K$  single-antenna users. The ELAA consists of a UPA with  $M$  elements, which are arranged in the  $yz$ -plane with  $M_y$  and  $M_z$  elements on the horizontal ( $y$ -axis) and vertical ( $z$ -axis) axes, respectively, such that  $M = M_y \cdot M_z$ . At the ELAA, the frequency-domain precoded vector signal is mapped to the time domain by performing an inverse discrete Fourier transform (IDFT) at each antenna element before being passed to a power amplifier which amplifies the transmitted time-domain signal.

More specifically, we denote the discrete-time input and output signals to the amplifiers at the  $m$ -th antenna element and time sample  $n$  as  $x_m[n]$  and  $y_m[n]$ , respectively, where  $m$  is the  $m = m_y M_z + m_z$  for  $m_y = 0, \dots, M_y - 1$  and  $m_z = 0, \dots, M_z - 1$ . By denoting the operation of the PA at the  $m$ -th element as  $\mathcal{A}(\cdot)$ <sup>1</sup>, the amplified transmit signal is given by

$$y_m[n] = \mathcal{A}(x_m[n]). \quad (1)$$

For later use, we introduce the  $M \times 1$  vector notation of the signals at the RIS before and after amplification at time sample

<sup>1</sup>All PAs among the ELAA elements are assumed to have the same transfer function. This fact can be seen as a worst case in terms of coherent combining of distortion [16]. Small manufacturing variations will have negligible impact on the end results [17].

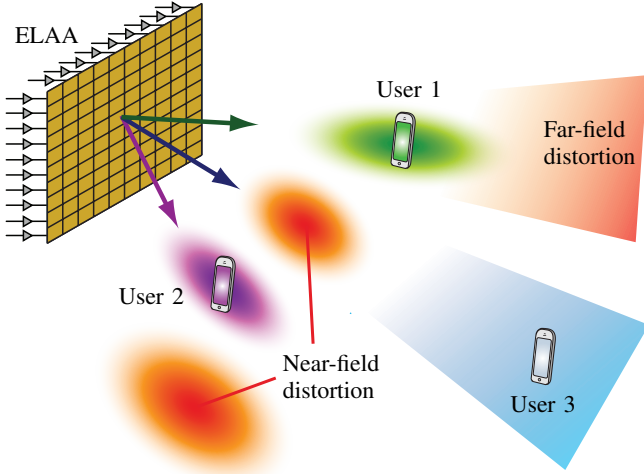


Fig. 1: The considered setup with an ELAA with  $M$  antennas that transmit user signals using power amplifiers that create nonlinear distortion, resulting in distortion focused at different places in the near- and far-field.

$n$  as  $\mathbf{x}_n = [x_1[n], \dots, x_M[n]]^T$  and  $\mathbf{y}_n = [y_1[n], \dots, y_M[n]]^T$ , respectively. For analytical tractability, we consider a third-order memoryless polynomial distortion model<sup>2</sup> for the PAs at the ELAA and RIS. Specifically,

$$\mathcal{A}(x_m[n]) = \beta_1 x_m[n] + \beta_3 x_m[n] |x_m[n]|^2, \quad (2)$$

where  $\beta_1, \beta_3 \in \mathbb{C}$  are the parameters for the first- and third-order term at the antenna elements.

The considered setup is illustrated in Fig. 1 where an ELAA transmits to three users, two located in the near-field and one in the far-field. The non-linear distortion in the power amplifiers will give rise to distortion that is focused at specific locations in the near- and far-field, which will be characterized in this paper.

#### A. Near- and Far-field Channel Models

We will now consider the radiative near-field and utilize the Fresnel region of the array response vector  $\mathbf{a}(\varphi, \theta, r)$  between a UPA of  $N$  identical antennas and a point of interest  $\psi = (\varphi, \theta, r)$ . Here,  $\varphi$  and  $\theta$  can specify either the incoming wave arrival direction from a user located at the point  $\psi$  or the outgoing wave direction from the UPA towards the point  $\psi$  in terms of azimuth and elevation angles, respectively. Additionally, the value  $r$  is the distance between the first element of the UPA (i.e.,  $m = 0$ ) and the point of interest  $\psi$ . The array response vector  $\mathbf{a}(\psi) \in \mathbb{C}^{M \times 1}$  can be expressed as

$$\mathbf{a}(\psi) = \left[ 1, e^{j \frac{2\pi}{\lambda}(r-r_2)}, \dots, e^{j \frac{2\pi}{\lambda}(r-r_M)} \right]^T, \quad (3)$$

where  $r_m$  ( $n = 1, \dots, M$ ) denotes the distance between the  $m$ -th element of the UPA and the point  $\psi$ , where  $r = r_1$ . Assuming that the first (that is, the reference) element of the UPA is placed at the origin of the Cartesian coordinate system,

<sup>2</sup>Notice, that a third-order model is a reasonably good model for many hardware components in practice [14].

i.e., at  $(0, 0, 0)$  and expressing the point of interest  $\psi$  in polar coordinates as  $\psi = (r \cos \varphi \cos \theta, r \sin \varphi \cos \theta, r \sin \theta)$ , we have

$$r_m = (r^2 + k_y^2(m) + k_z^2(m) - 2rk_z(m) \sin \theta - 2rk_y(m) \sin \varphi \cos \theta)^{1/2}, \quad (4)$$

where  $k_z(m) \triangleq \text{mod}(m, M_z)d_z$  and  $k_y(m) \triangleq \lfloor \frac{m}{M_z} \rfloor d_y$  are the horizontal and vertical coordinates of the  $m$ -th element, and  $\text{mod}$  is the modulo operator. Moreover,  $d_y$  and  $d_z$  are the horizontal and vertical inter-element spacing, respectively. For later use, we simplify the relative distance  $r - r_m$  using the first-order Taylor approximation, i.e.,  $\sqrt{1-x} \approx 1 - x/2$  which yields

$$\phi_m(\varphi, \theta, r) \triangleq r - r_m \quad (5)$$

$$\begin{aligned} &\approx \tilde{\phi}_m(\varphi, \theta, r) \\ &= k_z(m) \sin \theta + k_y(m) \sin \varphi \cos \theta \\ &\quad - \frac{k_y^2(m) + k_z^2(m)}{2r}. \end{aligned} \quad (6)$$

The expression (6) is called Fresnel approximation and describes the spherical waves as parabolic [18]. We will use this approximation for the analytical derivations of distortion's beamformed directions, but we will use the exact expression in (4) for numerical validation.

Furthermore, notice that the array response vector  $\mathbf{a}(\psi)$  in (3) can also be used when the point of interest  $\psi$  is in the far-field region. In this case, the distance  $r$  is considerably larger than the aperture of the UPA, i.e.,  $r \gg k_y^2(m) + k_z^2(m)$  and thus, the last term in (6) can be neglected. Therefore, we have  $\phi_m(\varphi, \theta, r) \approx k_z(m) \sin \theta + k_y(m) \sin \varphi \cos \theta$  and in this case the array response vector  $\mathbf{a}(\psi)$  becomes

$$\mathbf{a}(\varphi, \theta) = \left[ 1, \dots, e^{j \frac{2\pi}{\lambda}(k_z(m) \sin \theta + k_y(m) \cos \theta \sin \varphi)}, \dots, e^{j \frac{2\pi}{\lambda}(k_z(M) \sin \theta + k_y(M) \cos \theta \sin \varphi)} \right]^T, \quad (7)$$

which is independent of the distance  $r$  and the array response vector in the far-field region.

#### B. Linear Precoded Signal

At the ELAA, the data symbols for the  $K$  users are mapped to the antenna array by a precoder. We denote the transmitted symbol on subcarrier  $l$  and time sample  $n$  to user  $k$  ( $k = 1, \dots, K$ ) as  $s_k[n, l]$ , while the corresponding  $K \times 1$  data symbols vector is denoted as  $\mathbf{s}[n, l] = [s_1[n, l], \dots, s_K[n, l]]^T$ .

We assume that the ELAA has access to perfect channel state information (CSI), i.e., it has perfect knowledge of the realizations of the frequency-domain channel matrices  $\{\mathbf{H}_l\}$  for  $l \in \mathcal{S}$ . We make this assumption since the goal is to characterize the impact of nonlinear distortion. If the CSI is imperfect, the signals will be transmitted toward the wrong locations and the distortion will be determined by these believed user locations rather than the exact ones, but our results otherwise hold.

Notice that, in general, the channel at a given subcarrier is frequency flat and therefore the data symbols are precoded individually for each subcarrier by the precoder  $\mathbf{P}_l = \mathcal{P}(\mathbf{H}_l)$  which is frequency flat and a function  $\mathcal{P}: \mathbb{C}^{K \times M} \rightarrow \mathbb{C}^{M \times K}$

of the channel. That is, the  $M \times 1$  precoded symbol at time sample  $n$  is given by  $\mathbf{P}_l \mathbf{s}[n, l]$ . However, since the channel is line-of-sight (LoS), its frequency response is constant over frequency,  $\mathbf{H} = \mathbf{H}_l$  for  $l \in \mathcal{S}$ , and therefore the precoder becomes identical for all subcarriers, i.e.,  $\mathbf{P}_l = \mathbf{P}$  for  $l \in \mathcal{S}$ . The channel matrix is given by

$$\mathbf{H} = [\mathbf{a}(\varphi_1, \theta_1, r_1), \dots, \mathbf{a}(\varphi_K, \theta_K, r_K)]^T, \quad (8)$$

where  $\mathbf{a}(\cdot)$  is the array response vector defined in (3), while the ELAA observes the  $k$ -th user from the azimuth angle  $\varphi_k$ , elevation angle  $\theta_k$  and distance  $r_k$ .

Then, the OFDM time-domain vector  $\mathbf{x}_n$  before amplification at time sample  $n$  is obtained from the data symbols as

$$\mathbf{x}_n = \mathbf{P} \mathbf{s}_n, \quad (9)$$

where

$$\mathbf{s}_n \triangleq \frac{1}{\sqrt{N}} \sum_{l \in \mathcal{S}} \mathbf{s}[n, l] e^{j l \frac{2\pi}{N} n},$$

for  $n = 0, \dots, N-1$  represents the time-domain data symbols vector. The transmitted signal before the amplification  $\{\mathbf{x}_n\}$  satisfies the average transmit power constraint

$$\mathbb{E} \left[ \sum_{n=0}^{N-1} \|\mathbf{x}_n\|^2 \right] \leq PS, \quad (10)$$

where  $0 < P < \infty$  is the average transmit power at the base station and  $S \leq N$  is the number of occupied subcarriers.

Let  $\alpha_{mk} e^{j\phi_m(\varphi_k, \theta_k, r_k)}$  be the  $(m, k)$ -th entry of  $\mathbf{P}$ , i.e., the value of the precoder at the  $m$ -th antenna intended for the  $k$ -th user, where  $\alpha_{mk} \in \mathbb{R}$  and  $\phi_m(\cdot, \cdot, \cdot) \in \mathbb{R}$  denote the amplitude and phase of the precoder at the  $(m, k)$ -th entry. Then, from (9), the transmitted symbol before amplification at the  $m$ -th antenna element can be expressed as

$$x_m[n] = \sum_{k=1}^K \alpha_{mk} e^{-j \frac{2\pi}{\lambda} \phi_m(\varphi_k, \theta_k, r_k)} s_k[n], \quad (11)$$

where  $s_k[n]$  is the  $k$ -th entry of the vector  $\mathbf{s}_n$ , i.e., the time-domain symbol intended for the  $k$ -th user. For simplicity, we assume the maximum-ratio transmission (MRT) precoder. On this basis, since we assume a LoS channel, the phase of the precoder  $\phi_m(\cdot, \cdot, \cdot)$  is a conjugate match of the channel's phase. In this case, the transmitted signal  $x_m[n]$  is focused at the points  $(\varphi_k, \theta_k, r_k)$  for  $k = 1, \dots, K$ .

### III. NONLINEAR DISTORTION ANALYSIS

We are interested in the spatial characteristics of the third-order nonlinear term (or distortion) in (2) radiated from an ELAA. In the next theorem, we analytically derive the Fresnel approximation for the azimuth angle, elevation angle, and range of the near-field third-order distortion.

**Theorem 1.** *Suppose the baseband signal in (11) is passed through the non-linear function in (2). Then, the radiative near-field radiation pattern of the third-order non-linear distortion*

*is beamformed in a multitude of directions  $(\varphi_{pqv}, \theta_{pqv}, r_{pqv})$  approximated analytically by*

$$\theta_{pqv} \approx \arcsin(\sin \theta_p - \sin \theta_q + \sin \theta_v) \quad (12)$$

$$\varphi_{pqv} \approx \arcsin \left( \frac{1}{\cos \theta_{pqv}} (\cos \theta_p \sin \varphi_p - \cos \theta_q \sin \varphi_q + \cos \theta_v \sin \varphi_v) \right) \quad (13)$$

$$r_{pqv} \approx \left( \frac{1}{r_p} - \frac{1}{r_q} + \frac{1}{r_v} \right)^{-1} \quad (14)$$

for  $p, q, v = 1, \dots, K$ , where  $\varphi_{pqv} \in [-\frac{\pi}{2}, \frac{\pi}{2}]$ ,  $\theta_{pqv} \in [-\frac{\pi}{2}, \frac{\pi}{2}]$  and  $r_{pqv} \geq 0$  are the azimuth, elevation and range of each focal point, respectively.

*Proof:* See Appendix A. ■

The error of the Fresnel approximation used in Theorem 1 is small when  $-2\tilde{\phi}_m(\varphi, \theta, r)/r \leq 0.1745$ , which results in errors below  $3.5 \cdot 10^{-3}$  [19], [20, cf. expression (12)]. In practice, this can be achieved when the distance between the ELAA and a user is approximately at least 6 meters. Theorem 1 can also be generalized when  $K_{\text{FF}} (0 < K_{\text{FF}} \leq K)$  of the served users are in the far-field. With the next corollary we consider the extreme case where all users are in the far-field region.

**Corollary 1.** *Assuming that all users are in the far-field region ( $K_{\text{FF}} = K$ ), i.e.,  $r_k \rightarrow \infty \forall k$ , the elevation and azimuth directions of the radiated distortion are given by the expressions (12) and (13), respectively. The expression for the  $r_{pqv}$  in (14) is ignored since it does not have physical meaning for far-field channels.*

In the more general case where  $K_{\text{FF}} < K$  users are in the far-field, then as Corollary 1 implies the directions of elevation and azimuth in expressions (12) and (13), respectively, are valid regardless of whether a user is in the far- or near-field region. On the other hand, the expression for the near-field range  $r_{pqv}$  in (14) is modified depending on which users are in the far-field region. To illustrate this, let  $\mathcal{K}_{\text{FF}}$  be the set of users that are in the far-field region. Then,  $\forall k \in \mathcal{K}_{\text{FF}}$  the corresponding term  $1/r_k$  ( $k = 1, \dots, K$ ) in (14) is ignored.

Moreover, notice that the focal points  $(\varphi_{pqv}, \theta_{pqv}, r_{pqv})$  given in Theorem 1 are not unique. For instance, it is easy to see that  $(\varphi_{ppq}, \theta_{ppq}, r_{ppq}) = (\varphi_{vvq}, \theta_{vvq}, r_{vvq})$ ,  $\forall p, q, v$ . Thus, with the next corollary, we provide all the unique focal points derived in Theorem 1.

**Corollary 2.** *Let  $\mathcal{P}$  be the set of all unique focal points of the third-order non-linear distortion derived in Theorem 1. Then,  $\mathcal{P}$  is given as the union  $\mathcal{P} = \mathcal{P}_1 \cup \mathcal{P}_2 \cup \mathcal{P}_3$  of the following three disjoint subsets*

$$\mathcal{P}_1 = \{(\varphi_p, \theta_p, r_p) : p = 1, \dots, K\}, \quad (15)$$

$$\mathcal{P}_2 = \{(\varphi_{ppq}, \theta_{ppq}, r_{ppq}) : p, q = 1, \dots, K, q \neq p, K \geq 2\}, \quad (16)$$

$$\mathcal{P}_3 = \{(\varphi_{pqv}, \theta_{pqv}, r_{pqv}) : p, q, v = 1, \dots, K, q \neq p, v \neq p, v > q, K \geq 3\}. \quad (17)$$

*Proof: See Appendix B.* ■

It is worth mentioning that when the argument of the function  $\arcsin(\cdot)$  in (12) and (13) belongs to the subset of real numbers:  $(-\infty, -1) \cup (1, \infty)$ , then its corresponding value ( $\theta_{pqv}$  or  $\varphi_{pqv}$ ) is a complex number. In this case, the direction lacks a physical meaning and thus, it can be ignored since there is no physical location where the distortion can arise. Similarly, we consider only non-negative values of the range  $r_{pqv}$ . Therefore, the number of distortion directions of each subset in Corollary 2 are at most  $|\mathcal{P}_1| \leq K$ ,  $|\mathcal{P}_2| \leq K(K-1)$  and  $|\mathcal{P}_3| \leq K(K-1)(K-2)/2$  which implies that the total number of unique focal points are at most  $|\mathcal{P}| \leq (K^3 - K^2 + 2K)/2$ . This is in contrast to [12, Th. 2], where it is stated that the third-degree distortion is beamformed exactly into  $(K^3 - K^2 + 2K)/2$  directions.

Theorem 1 brings important insights into the characteristics of nonlinear distortion. First, notice that the distance (or range) of users from the ELAA does not affect the distortion on the elevation or azimuth angles. For example, when an ELAA performs finite-depth beamforming, i.e., all co-scheduled users are in the same direction but different distances from the ELAA, i.e., at  $(\varphi, \theta, r_k), \forall k$ , the distortion is beamformed towards the same direction but it is spread into distinct distances different from those of users according to the expression (14). Therefore, the distortion can have higher performance degradation in finite-depth beamforming than full-dimensional beamforming. The reason is that in finite-depth beamforming the distortion's radiation power is limited towards only one direction, while in full-dimensional beamforming, it is spread over the whole space resulting in lower power levels per directions.

With the next corollaries, we highlight two special cases of how the distortion is radiated in the azimuth and elevation domain in the  $yz$ -plane.

**Corollary 3.** *Suppose all users are located in the same elevation direction (i.e.,  $\theta_k = \theta_o, \forall k$ ) but different azimuth angles. The distortion is then focused at the points  $(\varphi_{pqv}, \theta_{pqv}, r_{pqv})$ :*

$$\theta_{pqv} \approx \theta_o, \quad (18)$$

$$\varphi_{pqv} \approx \arcsin(\sin \varphi_p - \sin \varphi_q + \sin \varphi_v), \quad (19)$$

and the distance  $r_{pqv}$  is given in the expression (14).

According to Corollary 3, the distortion is beamformed into the same elevation angle as that of the desired signal from the ELAA but in distinctly different directions in the azimuth domain. Furthermore, the azimuth directions are independent of the elevation angles of the users.

**Corollary 4.** *Suppose all users are located in the same azimuth direction (i.e.,  $\varphi_k = \varphi_o, \forall k$ ) but different elevation angles. Then, the distortion is beamformed into the directions  $(\varphi_{pqv}, \theta_{pqv}, r_{pqv})$ :*

$$\theta_{pqv} \approx \arcsin(\sin \theta_p - \sin \theta_q + \sin \theta_v), \quad (20)$$

$$\varphi_{pqv} \approx \arcsin\left(\frac{\sin \varphi_o}{\cos \theta_{pqv}} (\cos \theta_p - \cos \theta_q + \cos \theta_v)\right), \quad (21)$$

and the distance  $r_{pqv}$  is given in the expression (14).

According to Corollary 4, the ELAA can create distortion

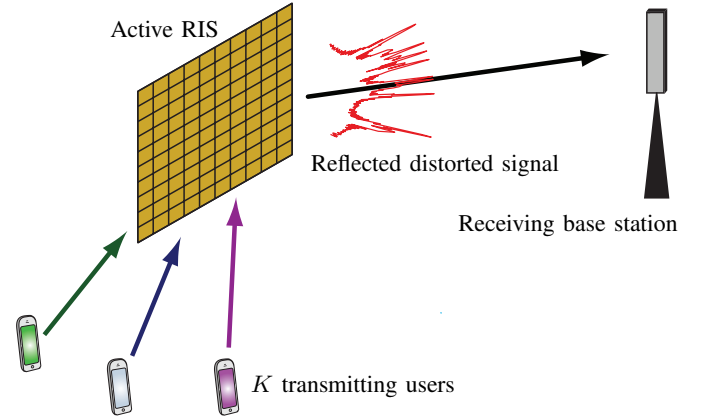


Fig. 2: The considered setup with an active RIS with  $N$  elements that reflects user signals toward a base station while creating nonlinear distortion.

which is beamformed into distinct directions different from those of the desired signals, and these are spread over both the azimuth and elevation domains. In particular, the azimuth direction is a function of the elevation implying that at different elevation angles, the distortion is beamformed towards different azimuth directions. Only when  $\varphi_o = 0^\circ$ , the distortion in the azimuth domain becomes independent of the elevation angles and it is beamformed into the zero angle.

Finally, it is worth mentioning that in the special case where the elevation angle  $\theta_o$  in Corollary 3 and the azimuth angle  $\varphi_o$  in Corollary 4 are zero, then the distortion's directions in (19) and (20), respectively, become identical with those of a ULA and therefore these corollaries coincide with [12, Th. 2].

#### IV. NONLINEAR DISTORTION OF AN ACTIVE RIS

We now consider an active RIS with  $N$  reconfigurable elements with the same geometric array structure as in the previous sections. It is deployed to beamform the impinging signal from  $K$  single-antenna users to a base station. At the RIS, the time-domain signal received from the users at each reflecting element is phase-shifted and then amplified before being re-radiated.<sup>3</sup> These amplifiers are nonlinear and this results in a reflected signal that is beamformed towards more locations than there are users, as illustrated in Fig. 2.

##### A. Phase-shifted Signal

We let the vector  $\mathbf{s}_n \in \mathbb{C}^{K \times 1}$  contain the transmitted time-domain OFDM symbols from the  $K$  users and the matrix  $\mathbf{G} \in \mathbb{C}^{M \times K}$  be the channel between the RIS and users. The impinging signal at the RIS will then be  $\mathbf{G}\mathbf{s}_n$ , while the phase-shifted signal  $\mathbf{x}_n$  at time sample  $n$  can be expressed as

$$\mathbf{x}_n = \mathbf{\Phi}\mathbf{G}\mathbf{s}_n, \quad (22)$$

where the diagonal matrix  $\mathbf{\Phi}$  with unit-modulus entries contains the RIS phase shift configuration. Since the users are assumed

<sup>3</sup>The order of phase-shifting and amplification has no impact on our results.

to have LoS channels to the RIS, the matrix  $\mathbf{G}$  can be written as

$$\mathbf{G} = [\mathbf{a}(\varphi_1, \theta_1, r_1), \dots, \mathbf{a}(\varphi_K, \theta_K, r_K)], \quad (23)$$

where  $\mathbf{a}(\cdot)$  is the array response vector defined in (3) and the RIS observes the  $k$ -th user from the azimuth angle  $\varphi_k$ , elevation angle  $\theta_k$  and distance  $r_k$ . We will denote the phase-shift in the  $m$ -th entry in (3) as

$$\frac{2\pi}{\lambda} \phi_m(\varphi, \theta, r), \quad (24)$$

and assume that the RIS is configured as

$$\Phi = \text{diag} \left( e^{-j \frac{2\pi}{\lambda} \phi_1(\varphi_s, \theta_s, r_s)}, \dots, e^{-j \frac{2\pi}{\lambda} \phi_M(\varphi_s, \theta_s, r_s)} \right), \quad (25)$$

to compensate for the phase-shifts for a signal arriving from the direction  $(\varphi_s, \theta_s, r_s)$ . The phase-shifted signal in (22) becomes

$$\mathbf{x}_n = \Phi \sum_{k=1}^K \mathbf{a}(\varphi_k, \theta_k, r_k) s_k[n], \quad (26)$$

where  $s_k[n]$  is the  $k$ -th entry of the vector  $\mathbf{s}_n$  and is the time-domain symbol transmitted by the  $k$ -th user. Hence, the phase-shifted signal at the  $m$ -th element before amplification is

$$x_m[n] = \sum_{k=1}^K e^{j \frac{2\pi}{\lambda} (\phi_m(\varphi_k, \theta_k, r_k) - \phi_m(\varphi_s, \theta_s, r_s))} s_k[n], \quad (27)$$

where  $\phi_m(\varphi, \theta, r)$  is defined in (5). We notice in (27) that the effective phase of the  $k$ -th signal after applying the RIS phase shifting is  $\phi_m(\hat{\varphi}_k, \hat{\theta}_k, \hat{r}_k) = \phi_m(\varphi_k, \theta_k, r_k) - \phi_m(\varphi_s, \theta_s, r_s)$ , where the effective azimuth angle  $\hat{\varphi}_k$ , elevation angle  $\hat{\theta}_k$  and range  $\hat{r}_k$  can be approximated analytically

$$\hat{\theta}_k \approx \arcsin(\sin \theta_k - \sin \theta_s), \quad (28)$$

$$\hat{\varphi}_k \approx \arcsin \left( \frac{1}{\cos \hat{\theta}_k} (\cos \theta_k \sin \varphi_k - \cos \theta_s \sin \varphi_s) \right), \quad (29)$$

$$\hat{r}_k \approx \frac{r_s r_k}{r_s - r_k}, \quad r_s \neq r_k \quad (30)$$

by using the Fresnel approximation of  $\phi_m(\cdot, \cdot, \cdot)$  in (6). Notice from (6), that in the case of  $r_s = r_k$ , the phase of the re-directed signal, i.e.,  $\phi_m(\varphi_k, \theta_k, r_k) - \phi_m(\varphi_s, \theta_s, r_s)$  is independent of the distances  $r_s$  and  $r_k$  implying that the re-transmitted signal does not have a focal point in the near-field region but in far-field.

Without the RIS phase-shifts (i.e., if they are zero), the  $k$ -th signal arrives from  $(\varphi_k, \theta_k)$  and would be reflected (mainly) towards the direction  $(-\varphi_k, -\theta_k)$ . With the RIS phase-shifts, the signal is instead reflected in the direction  $(-\hat{\varphi}_k, -\hat{\theta}_k)$ .

### B. Nonlinear Distortion

With the next corollary we provide the spatial characteristics of the third-order nonlinear term (or distortion) radiated from an active RIS.

**Corollary 5.** *Suppose the baseband signal in (27) is passed through the non-linear function in (2). Then, the radiation pattern of the third-order non-linear distortion is beamformed*

*in a multitude of directions  $(-\varphi_{pqv}, -\theta_{pqv}, r_{pqv})$  approximated analytically by*

$$\theta_{pqv} \approx \arcsin \left( \sin \hat{\theta}_p - \sin \hat{\theta}_q + \sin \hat{\theta}_v \right), \quad (31)$$

$$\varphi_{pqv} \approx \arcsin \left( \frac{1}{\cos \theta_{pqv}} \left( \cos \hat{\theta}_p \sin \hat{\varphi}_p - \cos \hat{\theta}_q \sin \hat{\varphi}_q + \cos \hat{\theta}_v \sin \hat{\varphi}_v \right) \right), \quad (32)$$

$$r_{pqv} \approx \left( \frac{1}{\hat{r}_p} - \frac{1}{\hat{r}_q} + \frac{1}{\hat{r}_v} \right)^{-1}, \quad (33)$$

for  $p, q, v = 1, \dots, K$ , where  $\varphi_{pqv} \in [-\frac{\pi}{2}, \frac{\pi}{2}]$ ,  $\theta_{pqv} \in [-\frac{\pi}{2}, \frac{\pi}{2}]$  and  $r_{pqv} \geq 0$  are the azimuth, elevation and range of each point, respectively.

Notice that Corollary 5 is identical with Theorem 1. Therefore, the behavioural analysis derived in Theorem 1 for an ELAA system, it can be also applied for an active RIS. However, in the latter case, the beamformed vector of each signal is not created in the baseband but comes from the channel from the users as well as we can modify the reflected angles using the RIS.

## V. NUMERICAL RESULTS

In this section, we present simulation results to validate our theoretical analysis and the tightness of the approximations. We consider that both ELAA and RIS are equipped with a UPA with half-wavelength antenna spacing. The parameters of the nonlinear PA model in (2) are chosen such that the error vector magnitude at the output is 3%, i.e.,  $\beta_1 = 1.042$  and  $\beta_3 = -0.0212$ . Moreover, without loss of generality, we assume that the RIS phase shifter rotates the impinging signal by  $(\varphi_s, \theta_s) = (-2^\circ, -4^\circ)$  to target the base station.

### A. Near- and Far-Field Distances for Antenna Arrays

The near-field can be divided into reactive and radiative, where the latter is also known as Fresnel region. The radiative near-field starts at the Fresnel distance [19]. Furthermore, the radiative near-field and far-field are separated by the Fraunhofer array distance  $d_{\text{FA}} = \frac{2\Delta^2}{\lambda}$ , where  $\Delta$  is the maximum linear dimension of the array and  $\lambda$  is the wavelength. We are interested in the radiative near-field region where there exists only phase variation over the array, characterized by spherical wavefronts. This region occurs when the propagation distance is larger than  $d_B = 2\Delta$  but smaller than  $d_{\text{FA}}$  [19], [20].

In this section, we assume that the carrier frequency is 3GHz, the antenna spacing is  $\lambda/2$  and the UPA has the same number of elements per dimension, i.e.,  $M_z = M_y = M_o$ . Therefore, its maximum linear dimension is  $\Delta = \lambda(M_o - 1)/\sqrt{2}$ , where  $\lambda = 0.1$  meters. In the case, we have a UPA with  $20 \times 20$  elements, the radiative near-field starts at  $d_B = 2.68$  meters and it ends at the propagation distance  $d_{\text{FA}} = 36.1$  meters. When the propagation distance is larger than 36.1 m, the wavefront can be characterized by a planar wavefront, as observed in the far-field model. When the size of the UPA increases to  $35 \times 35$

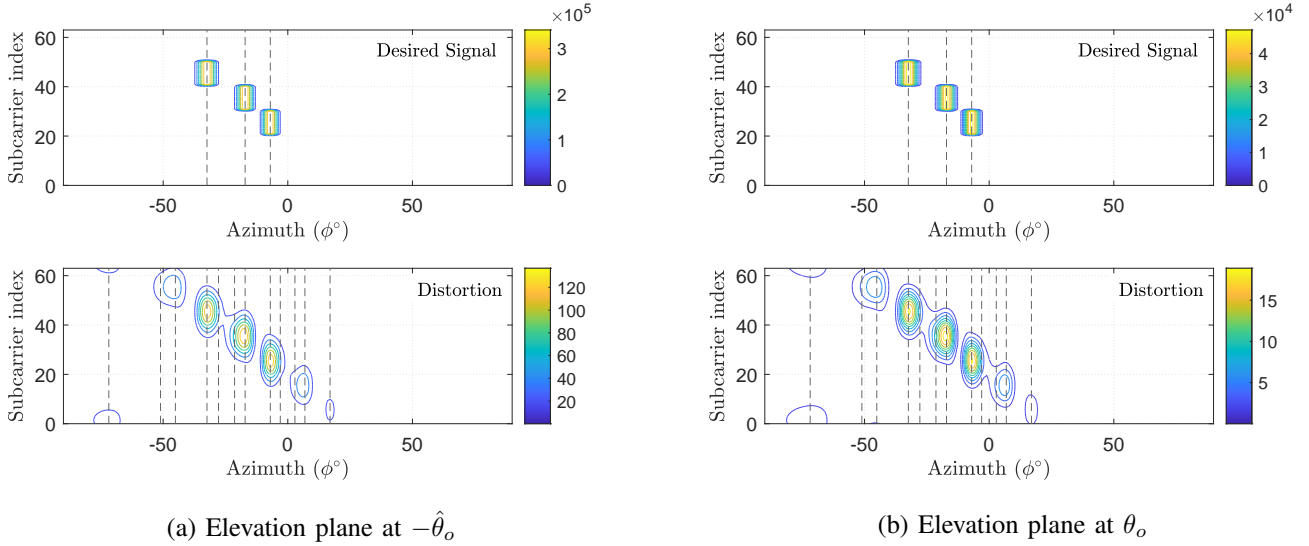


Fig. 3: The PSD of the far-field linear signal (top) and nonlinear distortion (bottom) radiated from an active RIS with  $20 \times 20$  antenna elements as a function of the subcarrier index and azimuth angle. All users are seen from the same elevation angle of  $\theta_o = 0^\circ$ . The vertical lines represent the theoretical azimuth directions of the distortion obtained in Theorem 1.

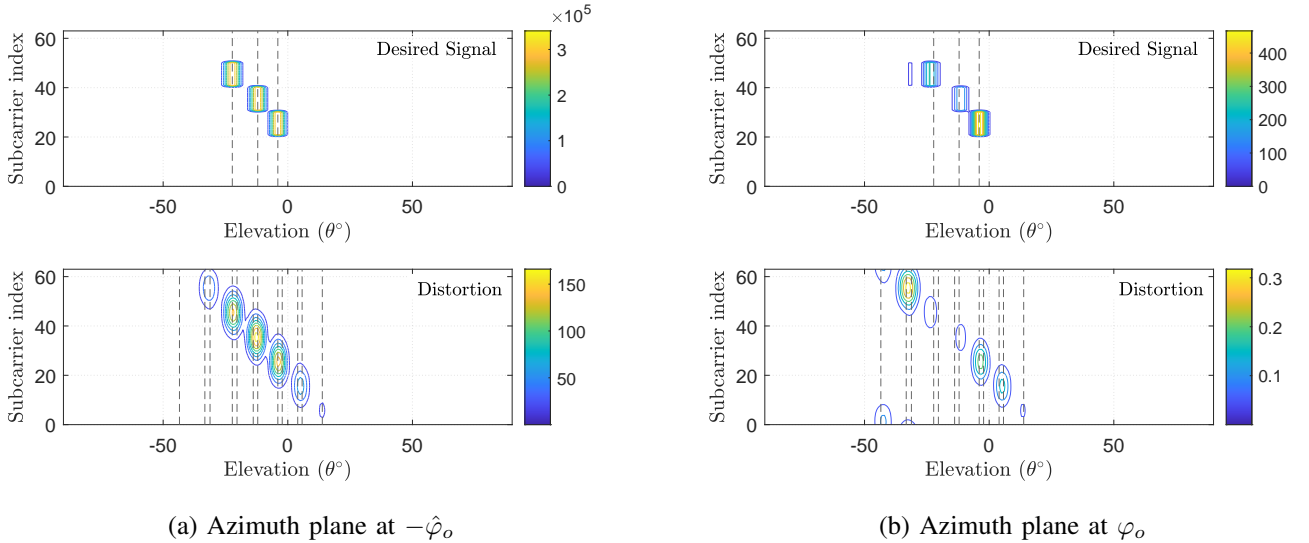


Fig. 4: The PSD of the far-field linear signal (top) and nonlinear distortion (bottom) radiated from an active RIS with  $20 \times 20$  antenna elements as a function of the subcarrier index and elevation angle. All users are seen from the same azimuth angle of  $\varphi_o = 14^\circ$ . The vertical lines represent the theoretical elevation directions of the distortion obtained in Theorem 1.

elements, then the radiative near-field starts at  $d_B = 4.8$  meters and it ends at the propagation distance  $d_{FA} = 115.6$  meters.

### B. Radiation Pattern

To demonstrate the radiation patterns of the desired (linear) signal and nonlinear distortion, we use the Bussgang decomposition [21] to express the output of the PAs as

$$\mathbf{y}_n = \mathcal{A}(\mathbf{x}_n) = \mathbf{G}\mathbf{x}_n + \mathbf{d}_n, \quad (34)$$

where the scaled desired signal  $\mathbf{u}_n \triangleq \mathbf{G}\mathbf{x}_n$  is the linear part of the output and the nonlinear distortion is represented by  $\mathbf{d}_n \in \mathbb{C}^{M \times 1}$ , which is uncorrelated with  $\mathbf{x}_n$ . For the considered

third-order memoryless PA, the Bussgang gain matrix  $\mathbf{G} = \mathbf{I}_M + 2\beta_3 \text{diag}(\mathbf{C}_{yy}[0])$  is a diagonal matrix, where  $\mathbf{C}_{xx}[\tau] = \mathbb{E}\{\mathbf{x}_n \mathbf{x}_n^H[-\tau]\}$  is the covariance matrix of  $\mathbf{x}_n$ . Similarly, the covariance matrix of the distortion vector is given by  $\mathbf{C}_{dd}(\tau) = \mathbf{C}_{yy}[\tau] - \mathbf{C}_{uu}[\tau]$ , where  $\mathbf{C}_{uu}[\tau] = \mathbf{G}\mathbf{C}_{xx}[\tau]\mathbf{G}$  and the output covariance  $\mathbf{C}_{yy}[\tau]$  is given analytically in [22, Eq. (27)].

The radiation pattern in the frequency domain is given by the power spectral density (PSD)  $\mathbf{S}_{yy}(f)$ , which is found by taking the Fourier transform of  $\mathbf{C}_{yy}[\tau]$ . Then, the power radiated in the direction of  $(\varphi, \theta)$  at frequency  $f$  is obtained by multiplying by the corresponding array response vector:

$$\mathbf{S}_{\varphi, \theta, r}(f) = \mathbf{a}^T(\varphi, \theta, r) \mathbf{S}_{yy}(f) \mathbf{a}^*(\varphi, \theta, r). \quad (35)$$

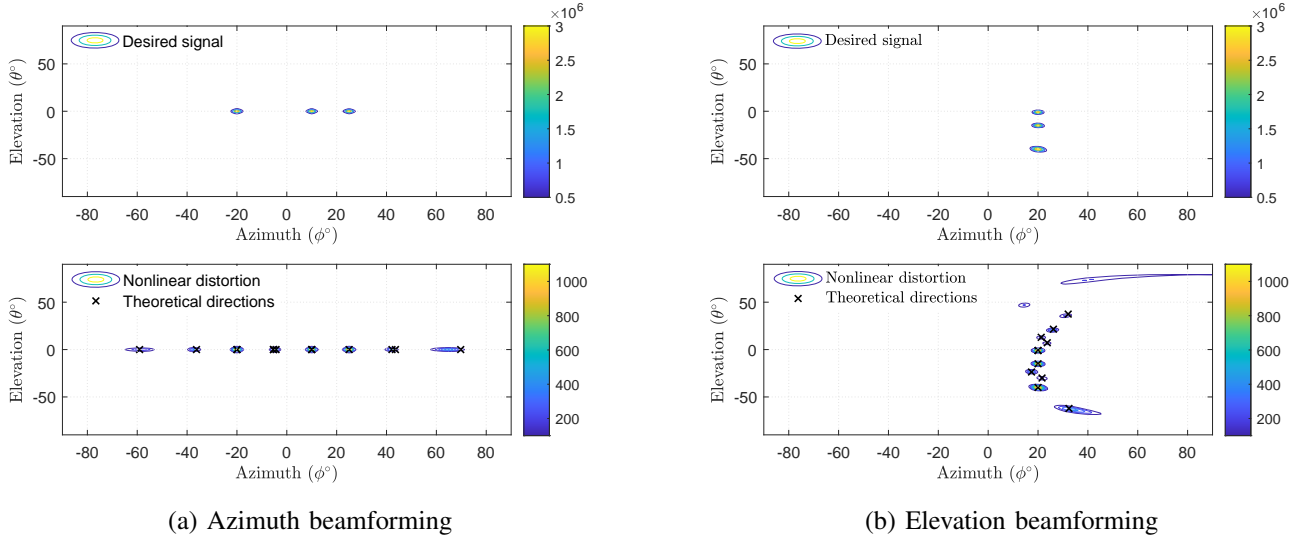


Fig. 5: The PSD of the radiative near-field linear signal (top) and nonlinear distortion (bottom) for three different cases of users position. In this example, we assume a UPA  $35 \times 35$ , carrier frequency  $f = 3$  GHz. In all cases, all users are located at the range of 20m from the ELAA.

To distinguish the desired linear signal from the undesired nonlinear distortion, we use the decomposition in (34). Since the useful signal and distortion terms are uncorrelated, the PSD of the transmitted signal can be expressed as

$$\mathbf{S}_{yy}(f) = \mathbf{S}_{uu}(f) + \mathbf{S}_{dd}(f),$$

where  $\mathbf{S}_{uu}(f)$  and  $\mathbf{S}_{dd}(f)$  can be computed by taking the Fourier transforms of  $\mathbf{C}_{uu}[\tau]$  and  $\mathbf{C}_{dd}[\tau]$ , respectively. The radiation patterns of the in-band desired signal and in-band/out-of-band nonlinear distortion can be computed as  $\mathbf{a}^T(\varphi, \theta, r) \mathbf{S}_{uu}(f) \mathbf{a}^*(\varphi, \theta, r)$  and  $\mathbf{a}^T(\varphi, \theta, r) \mathbf{S}_{dd}(f) \mathbf{a}^*(\varphi, \theta, r)$ , respectively, by following the same principle as in (35).

### C. Distortion in the Frequency-Azimuth Domain

In Fig. 3, we show the PSD of the radiated signal from the RIS when it receives far-field signals from three users that are seen from the same elevation angle ( $\theta_o = 0^\circ$ ) but in different azimuth angles:  $(\varphi_1, \varphi_2, \varphi_3) = (2^\circ, 20^\circ, 35^\circ)$ . Each user allocates a different set of subcarriers as shown in Fig. 3, and might be served by the same base station or a different one.

In Fig. 3(a), we show the PSD of the desired signal (top) and nonlinear distortion (bottom) as a function of the subcarrier index and azimuth angle. Since the radiated field is three-dimensional, we consider the elevation plane that the RIS focuses the signals towards (i.e.,  $\hat{\theta}_o$ ). We notice that the RIS creates both in-band and out-of-band distortion that is beamformed into distinct directions; there are more directions than the number of users and distortion appears in bands where the desired signal does not exist. Nevertheless, most of the distortion power is beamformed in the same directions as the desired signal. Additionally, in Fig. 3(b), we show the same functions but consider the original elevation plane where

the users reside (i.e.,  $\theta_o$ ). As expected, we notice that the distortion is stronger towards the direction of the re-radiated signal, where the RIS signal is beamformed, than in the original plane. Moreover, we notice that as long as all users are located at the same elevation angle, the azimuth beamforming directions of the distortion are not affected by which elevation plane we consider. This is a consequence of Corollary 3, which proves that the distortion radiated from the RIS is beamformed only in the azimuth domain. Finally, we notice that the theoretical distortion directions derived in Corollary 3 (shown as vertical lines) coincide with those obtained by the simulations.

### D. Distortion in the Frequency-Elevation Domain

Similarly, in Fig. 4, we show the PSD of the radiated signal from the RIS when it receives far-field signals from three users seen from the same azimuth angle (i.e.,  $\varphi_o = 14^\circ$ ) but in different elevation angles  $(\theta_1, \theta_2, \theta_3) = (1^\circ, 8^\circ, 18^\circ)$ .

In Fig. 4(a), we show the PSD of the desired signal (top) and nonlinear distortion (bottom) as a function of the subcarriers index and elevation angle in the azimuth plane that the re-radiated signal is aimed towards using the RIS. By contrast, in Fig. 4(b), we consider the original azimuth plane in the direction of the users. A main difference from Fig. 3 is that the elevation beamforming directions of the distortion depend on the azimuth direction. In other words, different azimuth directions yield different beamforming directions of the distortion in the elevation domain. For example, we notice that in Fig. 4(a), some of the elevation beamforming directions of the distortion derived in Corollary 4 are missing. The reason is that these elevation directions appear at different azimuth directions as shown in Fig. 4(b).

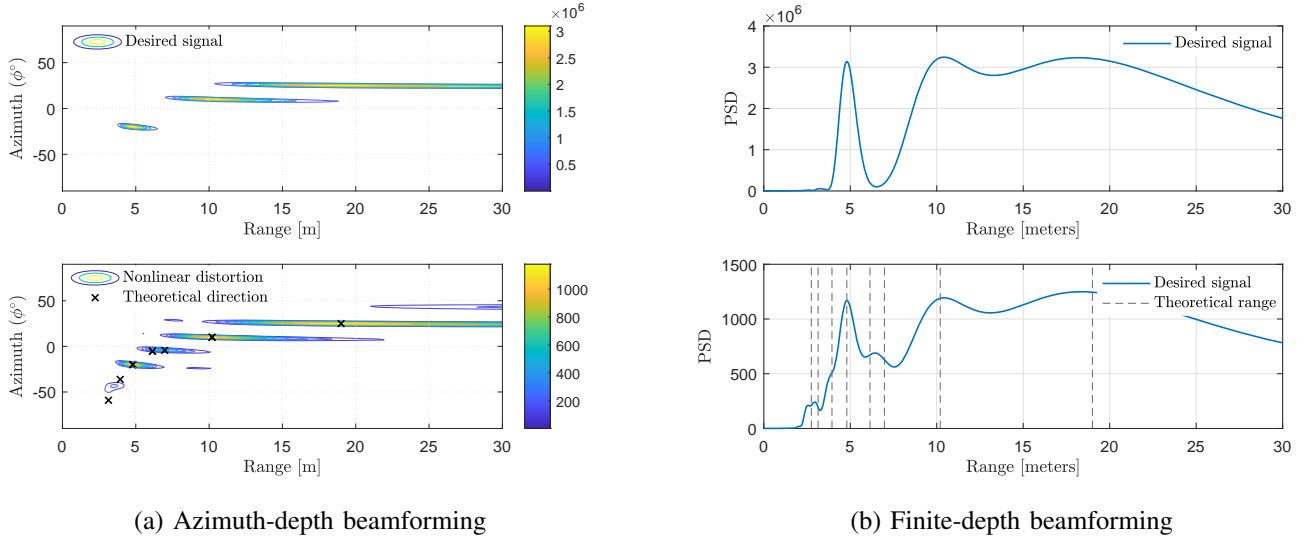


Fig. 6: The PSD of the radiative near-field linear signal (top) and nonlinear distortion (bottom) radiated from an ELAA. In this example, we assume a UPA  $35 \times 35$  and carrier frequency  $f = 3$  GHz.

### E. Distortion in the Angular Domain

Next, we illustrate Theorem 1 by showing the PSD of nonlinear distortion as a function of the azimuth and elevation planes. To facilitate this, all users occupy the same subcarrier indices and they are located at the same distance from the ELAA ( $r_o = 20$ m). More precisely, in Fig. 5(a), we show the PSD of the desired signal (top) and nonlinear distortion (bottom) radiated from an ELAA towards three co-scheduled users as a function of the elevation and azimuth angles. We assume two-dimensional azimuth beamforming, that is all users are located at the same elevation angle (i.e.,  $\theta_o = 0^\circ$ ) but at different azimuth angles  $(\varphi_1, \varphi_2, \varphi_3) = (-20^\circ, 10^\circ, 25^\circ)$ .

As indicated in Corollary 3 the distortion is beamformed into the same elevation angle as that of the desired signals but at different azimuth directions. On the other hand, when we assume two-dimensional elevation beamforming, i.e., the users are located at the same azimuth (i.e.,  $\varphi_o = 20^\circ$ ) but at different elevation angles  $(\theta_1, \theta_2, \theta_3) = (-1^\circ, -15^\circ, -40^\circ)$  as shown in Fig. 5(b), the distortion will not only beamformed at different elevation angles than those of the desired signal but it will also spread at different azimuth angles than  $(\varphi_o)$  as proved in Corollary 4.

### F. Distortion in the Depth Domain

In Fig. 6(a), we assume that all three co-scheduled users occupy the same subcarrier indices and are located in the same elevation angle (i.e.,  $\theta_o = 0^\circ$ ). As it is shown in the the PSD of the desired signal (top), the distances to the users from the ELAA are  $(r_1, r_2, r_3) = (4.8, 9.8, 19)$  and it is seen from the azimuth angle  $(\varphi_1, \varphi_2, \varphi_3) = (-20^\circ, 10^\circ, 25^\circ)$ , respectively. First, notice that the nonlinear distortion is focused at distinct points that are at different azimuth and distances from the ELAA than those of the desired signal as predicted in Theorem 1. Additionally, notice that the azimuth directions of the users in

this example are the same as those in the example of Fig. 5(a). Thus, one would expect that the distortion's azimuth directions in these two examples are identical. However, in this example, due to the fact that the users are at different distances from the ELAA, the expression (14) for the distortion's distances yields negative values for some azimuth directions which do not appear in the PSD of the Fig. 6(a). Therefore, the distortion's focal points in Fig. 6(a) are less than those in Fig. 5(a).

Finally, in Fig. 6(b), we demonstrate the tightness of the approximate closed-form expression of focusing points of nonlinear distortion derived in Theorem 1. We assume finite-depth beamforming, that is, all three users are located at the same azimuth and elevation direction but at different near-field distances from the ELAA:  $(r_1, r_2, r_3)$ . Notice that the distortion can be beamformed into distinct distances different from those of the desired signal, while the approximation of Theorem 1 are very tight.

## VI. CONCLUSION

In this paper, we analyzed how ELAAs and active RISs with nonlinear amplifiers introduce distortion when transmitting signals. We analyzed the spatial distortion characteristics in the entire 3D space of radiative near-field channels, i.e., in the azimuth, elevation, and depth domains. We derived a new theorem that predicts the beamforming/focusing of the distortion, which match the directions/depths of the desired signals, but distortion also appears at many other distinct locations in the near- and far-field, when the co-scheduled users are located at different near-field distances from the ELAA or RIS. Furthermore, it was shown that when an ELAA transmits or an active RIS receives data signals from multiple users located in different elevation angle directions, the distortion spreads into distinct directions that involve both azimuth and elevation angles not present in the original signal. On the other hand, the azimuth positions of the users do not affect the

behavior of distortion in the elevation domain. The nonlinear distortion causes both in-band and out-of-band distortion since the signals expand in the frequency domain.

#### APPENDIX A PROOF OF THEOREM 1

In order to find the focal points of the third-order non-linear distortion, we express the radiation pattern of distortion in terms of array factor, i.e.,

$$\mathbf{AF}_3(\varphi, \theta, r) = \beta_3 \sum_{m=1}^M a_m(\varphi, \theta, r) x_m[n] |x_m[n]|^2, \quad (36)$$

where  $a_m(\cdot, \cdot, \cdot)$  is the LoS channel between the  $m$ -th antenna element and the point  $(\varphi, \theta, r)$ . Furthermore, in order to derive tractable analytical expressions for the beamforming directions and range of distortion, we approximate the channel (a.k.a. Fresnel approximation) as

$$a_m(\varphi, \theta, r) \approx e^{j \frac{2\pi}{\lambda} \tilde{\phi}_m(\varphi, \theta, r)}, \quad (37)$$

which is tight when the propagation distance is larger than the  $d_B = 2\Delta$  distance, where  $\Delta$  is the maximum linear dimension of the array and the amplitude variations between the point  $(\varphi, \theta, r)$  and the aperture of ELAA are negligible [19], [20].

Now, by substituting (27) and (37) into (36), we get the expression

$$\begin{aligned} \mathbf{AF}_3(\varphi, \theta, r) &\approx \beta_3 \sum_{p=1}^K \sum_{q=1}^K \sum_{v=1}^K s_p[n] s_q^*[n] s_v[n] \\ &\times \underbrace{\sum_{m=1}^M g_{mpqv} e^{-j \frac{2\pi}{\lambda} (\tilde{\phi}_m(\varphi, \theta, r) - \tilde{\phi}_m(\varphi_{pqv}, \theta_{pqv}, r_{pqv}))}}_{\triangleq \mathbf{AF}_{pqv}(\varphi, \theta, r)} \end{aligned} \quad (38)$$

where  $\varphi_{pqv}$ ,  $\theta_{pqv}$  and  $r_{pqv}$  are given by the expressions (13), (12) and (14), respectively and  $g_{mpqv} \triangleq a_{mp} a_{mq}^* a_{mv}$ . Assuming the array response vector in (3) and without loss of generality, we have  $g_{mpqv} = 1$ ,  $\forall m, p, q, v$ . Notice that the amplitude of the term  $\mathbf{AF}_{pqv}(\varphi, \theta, r)$  can be upper bounded using the generalized triangle inequality as

$$|\mathbf{AF}_{pqv}(\varphi, \theta, r)| \leq \sum_{m=1}^M \left| e^{-j \frac{2\pi}{\lambda} (\tilde{\phi}_m(\varphi, \theta, r) - \tilde{\phi}_m(\varphi_{pqv}, \theta_{pqv}, r_{pqv}))} \right|,$$

where the equality holds if and only if the channel vector equals that of the effective precoder, i.e.,

$$\tilde{\phi}_m(\varphi, \theta, r) = \tilde{\phi}_m(\varphi_{pqv}, \theta_{pqv}, r_{pqv}) \quad (39)$$

Therefore, the term  $|\mathbf{AF}_{pqv}(\varphi, \theta, r)|$  is maximized at the points where  $(\varphi, \theta, r) = (\varphi_{pqv}, \theta_{pqv}, r_{pqv})$  for  $p, q, v = 1, \dots, K$ .

#### APPENDIX B PROOF OF COROLLARY 1

The expression (38) can be re-written as

$$\begin{aligned} \mathbf{AF}_3(\varphi, \theta, r) &= (2K-1) \sum_{p=1}^K c_{ppp} \mathbf{AF}_{ppp}(\varphi, \theta, r) \\ &+ \sum_{p=1}^K \sum_{\substack{q=1 \\ p \neq q}}^K c_{pqp} \mathbf{AF}_{pqp}(\varphi, \theta, r) \\ &+ 2 \sum_{p=1}^K \sum_{\substack{q=1 \\ q \neq p}}^K \sum_{\substack{v=1 \\ v \neq p \\ v > q}}^K c_{pqv} \mathbf{AF}_{pqv}(\varphi, \theta, r) \end{aligned} \quad (40)$$

where

$$c_{pqv} \triangleq \beta_3 s_p[n] s_q^*[n] s_v[n] \quad (41)$$

Notice, that each term in (40) represents a unique radiation pattern stemming from nonlinear distortion. For example, the first, second and third term yields the focusing points for  $\mathcal{P}_1$ ,  $\mathcal{P}_2$  and  $\mathcal{P}_3$ , respectively.

#### REFERENCES

- [1] N. Kolomvakis and E. Björnson, "Nonlinear distortion issues created by active reconfigurable intelligent surfaces," in *EuCAP*, 2024.
- [2] E. Björnson, L. Sanguinetti, H. Wymeersch, J. Hoydis, and T. L. Marzetta, "Massive MIMO is a reality—what is next?: Five promising research directions for antenna arrays," *Digital Signal Processing*, vol. 94, pp. 3–20, 2019, special Issue on Source Localization in Massive MIMO.
- [3] C. Huang, A. Zappone, G. C. Alexandropoulos, M. Debbah, and C. Yuen, "Reconfigurable intelligent surfaces for energy efficiency in wireless communication," *IEEE Trans. Wireless Commun.*, vol. 18, no. 8, pp. 4157–4170, 2019.
- [4] M. Di Renzo, A. Zappone, M. Debbah, M. S. Alouini, C. Yuen, J. de Rosny, and S. Tretyakov, "Smart radio environments empowered by reconfigurable intelligent surfaces: How it works, state of research, and the road ahead," *IEEE J. Sel. Areas Commun.*, vol. 38, no. 11, pp. 2450–2525, 2020.
- [5] E. Björnson, O. Ozdogan, and E. G. Larsson, "Reconfigurable intelligent surfaces: Three myths and two critical questions," *IEEE Commun. Mag.*, vol. 58, no. 12, pp. 90–96, 2020.
- [6] Q. Wu, S. Zhang, B. Zheng, C. You, and R. Zhang, "Intelligent reflecting surface-aided wireless communications: A tutorial," vol. 69, no. 5, pp. 3313–3351, 2021.
- [7] E. Björnson, H. Wymeersch, B. Matthieson, P. Popovski, L. Sanguinetti, and E. de Carvalho, "Reconfigurable intelligent surfaces: A signal processing perspective with wireless applications," *IEEE Signal Process. Mag.*, vol. 39, no. 2, pp. 135–158, 2022.
- [8] Z. Zhang, L. Dai, X. Chen, C. Liu, F. Yang, R. Schober, and H. V. Poor, "Active RIS vs. passive RIS: Which will prevail in 6G?" *IEEE Trans. Commun.*, vol. 71, no. 3, pp. 1707–1725, 2023.
- [9] N. Kolomvakis, M. Matthaiou, and M. Coldrey, "IQ imbalance in multiuser systems: Channel estimation and compensation," *IEEE Trans. Commun.*, vol. 64, no. 7, pp. 3039–3051, 2016.
- [10] N. Kolomvakis, M. Coldrey, T. Eriksson, and M. Viberg, "Massive MIMO systems with IQ imbalance: Channel estimation and sum rate limits," *IEEE Trans. Commun.*, vol. 65, no. 6, pp. 2382–2396, 2017.
- [11] N. Kolomvakis, T. Eriksson, M. Coldrey, and M. Viberg, "Reconstruction of clipped signals in quantized uplink massive MIMO systems," *IEEE Trans. Commun.*, vol. 68, no. 5, pp. 2891–2905, 2020.
- [12] C. Mollén, U. Gustavsson, T. Eriksson, and E. G. Larsson, "Spatial characteristics of distortion radiated from antenna arrays with transceiver nonlinearities," *IEEE Trans. Wireless Commun.*, vol. 17, no. 10, pp. 6663–6679, 2018.
- [13] N. Kolomvakis, M. Bavand, I. Bahceci, and U. Gustavsson, "A distortion nullforming precoder in massive MIMO systems with nonlinear hardware," *IEEE Wireless Commun. Lett.*, vol. 11, no. 9, pp. 1775–1779, 2022.

- [14] E. G. Larsson and L. Van Der Perre, "Out-of-band radiation from antenna arrays clarified," *IEEE Wireless Commun. Lett.*, vol. 7, no. 4, pp. 610–613, 2018.
- [15] M. B. Salman, E. Björnson, G. M. Guvensen, and T. Ciloglu, "Analytical nonlinear distortion characterization for frequency-selective massive MIMO channels," in *IEEE ICC*, May 2023.
- [16] F. Rottenberg, G. Callebaut, and L. Van der Perre, "The z3ro family of precoders cancelling nonlinear power amplification distortion in large array systems," *IEEE Trans. Wireless Commun.*, vol. 22, no. 3, pp. 2036–2047, 2023.
- [17] C. Mollén, U. Gustavsson, T. Eriksson, and E. G. Larsson, "Impact of spatial filtering on distortion from low-noise amplifiers in massive MIMO base stations," *IEEE Trans. Wireless Commun.*, vol. 66, no. 12, pp. 6050–6067, 2018.
- [18] H. Do, N. Lee, and A. Lozano, "Parabolic wavefront model for line-of-sight MIMO channels," *IEEE Trans. Wireless Commun.*, vol. 22, no. 11, pp. 7620–7634, 2023.
- [19] E. Björnson and L. Sanguinetti, "Power scaling laws and near-field behaviors of massive MIMO and intelligent reflecting surfaces," *IEEE Open J. of the Commun. Soc.*, vol. 1, pp. 1306–1324, 2020.
- [20] A. Kosasih and E. Björnson, "Finite beam depth analysis for large arrays," <https://doi.org/10.48550/arXiv.2306.12367>, 2023.
- [21] Ö. T. Demir and E. Björnson, "The Bussgang decomposition of nonlinear systems: Basic theory and MIMO extensions," *IEEE Signal Process. Mag.*, vol. 38, no. 1, pp. 131–136, 2021.
- [22] C. Mollén, U. Gustavsson, T. Eriksson, and E. G. Larsson, "Out-of-band radiation measure for MIMO arrays with beamformed transmission," in *IEEE ICC*, 2016, pp. 1–6.

**Emil Björnson** (S'07-M'12-SM'17-F'22) is a Full Professor of Wireless Communication at the KTH Royal Institute of Technology, Sweden. He received an M.S. degree in engineering mathematics from Lund University, Sweden, in 2007, and a Ph.D. degree in telecommunications from KTH in 2011. From 2012 to 2014, he was a post-doc at the Alcatel-Lucent Chair on Flexible Radio, SUPELEC, France. From 2014 to 2021, he held different professor positions at Linköping University, Sweden. He was a Visiting Full Professor at KTH in 2020–2021, before obtaining a tenured position in 2022. He has authored the textbooks *Optimal Resource Allocation in Coordinated Multi-Cell Systems* (2013), *Massive MIMO Networks: Spectral, Energy, and Hardware Efficiency* (2017), and *Foundations of User-Centric Cell-Free Massive MIMO* (2021). He is dedicated to reproducible research and has made a large amount of simulation code publicly available. He performs research on MIMO communications, radio resource allocation, machine learning for communications, and energy efficiency. He is an Area Editor in *IEEE Signal Processing Magazine*. He has performed MIMO research for 17 years, his papers have received more than 25000 citations, and he has filed more than twenty patent applications. He is a host of the podcast *Wireless Future* and has a popular YouTube channel with the same name. He is an IEEE Fellow, a Wallenberg Academy Fellow, a Digital Futures Fellow, and an SSF Future Research Leader. He has received the 2014 Outstanding Young Researcher Award from IEEE ComSoc EMEA, the 2015 Ingvar Carlsson Award, the 2016 Best Ph.D. Award from EURASIP, the 2018 and 2022 IEEE Marconi Prize Paper Awards in Wireless Communications, the 2023 IEEE ComSoc Outstanding Paper Award, the 2019 EURASIP Early Career Award, the 2019 IEEE Communications Society Fred W. Ellersick Prize, the 2019 IEEE Signal Processing Magazine Best Column Award, the 2020 Pierre-Simon Laplace Early Career Technical Achievement Award, the 2020 CTTC Early Achievement Award, and the 2021 IEEE ComSoc RCC Early Achievement Award. He also co-authored papers that received Best Paper Awards at the conferences, including WCSP 2009, the IEEE CAMSAP 2011, the IEEE SAM 2014, the IEEE WCNC 2014, the IEEE ICC 2015, and WCSP 2017.

**Nikolaos Kolomvakis** undergraduate studies were in electronic and computer engineering at the Technical University of Crete, Greece. He obtained his M.Sc. degree in electrical engineering and information technology at the Swiss Federal Institute of Technology (ETH), Zurich, Switzerland, in 2012, and his Ph.D. degree in wireless communications at the Chalmers University of Technology, Gothenburg, Sweden, in 2019. From 2017 to 2023, he held the positions of a Systems Engineer and Senior Researcher at Ericsson AB in Stockholm, Sweden. From 2023, he is a postdoctoral researcher in the Division of Communication Systems at the KTH Royal Institute of Technology, Stockholm, Sweden. His research is in the area of wireless communications, electromagnetic information theory and signal processing, and he mainly focuses on developing theory, system modeling and designing hardware-aware algorithms for massive MIMO, holographic MIMO and large intelligent surfaces.

**Alva Kosasih** is a Postdoctoral researcher at KTH Royal Institute of Technology, Stockholm, Sweden. He holds a Ph.D. in communication engineering from the University of Sydney, Australia (2023). Alva received his B.Eng. and M.Eng. degrees in electrical engineering from Brawijaya University, Indonesia, in 2013 and 2017, respectively, and an M.S. degree in communication engineering from the National Sun Yat-sen University, Taiwan, in 2017. His research interests include signal processing for extra large-scale MIMO, near-field multiplexing and beamforming, MIMO decoding, and machine learning for the physical layer.